Journal of Environmental Chemical Engineering 12 (2024) 114059

Contents lists available at ScienceDirect

Journal of Environmental Chemical Engineering

journal homepage: www.elsevier.com/locate/jece

Influence of the ultrasound power density in the ultrasound-assisted synthesis of Ni-based LDH catalysts for CO_2 methanation

Michel Obeid [a,b], Christophe Poupin [a,*], Madona Labaki [b], Sharad Gupta [a], Samer Aouad [c,d], François Delattre [a], Ferdaous Ben Romdhane [e], François Devred [f], Eric M. Gaigneaux [f], Josefine Schnee [g], Edmond Abi-Aad [a]

[a] Unité de Chimie Environnementale et Interactions sur le Vivant, UR 4492, Univ. Littoral Côte d'Opale, 145 avenue Maurice Schumann, Dunkerque 59140, France
[b] Laboratory of Physical Chemistry of Materials (LCPM/PR2N), Lebanese University, Fanar, P.O. Box 90656, Jdeidet El Metn, Lebanon
[c] Department of Chemistry Faculty of Arts and Sciences, University of Balamand, Kelhat, Deir El Balamand, Lebanon
[d] Division of Science, New York University Abu Dhabi, Saadiyat Island, P.O. Box 129188, Abu Dhabi, UAE
[e] Sorbonne Université, CNRS, Fédération de Chimie et Matériaux de Paris-Centre, FCMat, PARIS F-75005, France
[f] Institute of Condensed Matter and Nanosciences (IMCN), Université catholique de Louvain, Pl. Louis Pasteur 1, L4.01.09, Louvain-la-Neuve 1348, Belgium
[g] Laboratoire de Réactivité de Surface (LRS), CNRS, Sorbonne Université, Campus Pierre et Marie Curie, 4 Place Jussieu, Cedex 05, Paris F-75005, France

ARTICLE INFO

Keywords:
Layered double hydroxide
Nickel
CO_2 methanation
Ultrasound
Power density

ABSTRACT

Ultrasound-assisted co-precipitation method was used to synthesize Ni-LDH based catalysts for CO_2 methanation. The influence of ultrasonic irradiation power density (90, 180, 270, and 360 $W{\cdot}L^{-1}$) on the physico-chemical properties of the catalysts as well as on their catalytic behavior was studied as compared to catalysts prepared by conventional co-precipitation. Based on the XRD results, ultrasound decreases the crystallite size of LDH structure whatever the power density used as compared to the conventional method, and by increasing the ultrasound power density, the crystallite size increases. This effect on dried samples leads to an increase in the size of nickel particles on the catalysts. 90 $W{\cdot}L^{-1}$ improves Ni particle distribution, catalyst basicity, and reducibility. Finally, Ni Us 90, the most performant catalyst in the studied series, shows a CO_2 conversion of 80 % and a CH_4 selectivity of 99.9 % at 350 ℃ with no deactivation for 100 hours under reaction conditions.

1. Introduction

Nowadays, society is largely dependent on fossil fuels, of whom the use creates severe environmental issues. The combustion of fossil fuels leads to the production of greenhouse gases, which are the primary cause of climate change [1]. The gradual depletion of fossil fuels and the environmental risks associated with their use requires the development of efficient and sustainable energy solutions such as solar power, wind power, and biomass-derived fuels [1]. Hydrogen produced from renewable energy sources like wind or photovoltaics, which has received a lot of attention in the sustainable energy society, is limited by its intermittency [2]. The end-user demand for power differs from the amount of electricity produced by renewable energy, suggesting a potential imbalance in the electrical network. A potential long-term and high-capacity renewable energy storage alternative is power-to-gas (PtG). This idea may be a promising approach to using extra electricity to electrolyze water to generate hydrogen gas [3]. However, hydrogen's low volume density and transportation challenges limit its use [3]. The formation of hydrocarbons and alcohols from CO_2 and hydrogen has therefore been widely studied to address the aforementioned problems [4]. The created fuels are also used to generate hydrogen at consumption locations and act as hydrogen storage media [4]. Methane serves as both a chemical feedstock and a fuel for gas turbines, which are used to produce electricity. Methane processing, storage, and transportation infrastructure are well developed because it is a significant part of natural gas [4]. The methanation reaction of CO_2, often known as the Sabatier reaction, works as follows:

$$CO_2 + 4\ H_2 \rightarrow CH_4 + 2\ H_2O\ \Delta H_{298} = -165\ kJ.mol^{-1} \quad (1)$$

Although this process is thermodynamically favorable, it remains kinetically limited [5]. An effective catalyst is required to accelerate the methanation reaction, which should demonstrate high activity, selectivity, and stability over a suitable temperature range, all while taking

* Corresponding author.
E-mail address: Christophe.poupin@univ-littoral.fr (C. Poupin).

https://doi.org/10.1016/j.jece.2024.114059
Received 13 May 2024; Received in revised form 23 August 2024; Accepted 3 September 2024
Available online 5 September 2024

into account economic considerations [6].

Several metals in the periodic table's group VIII, including Ni, Co, Fe, Ru, and Rh, are catalyzing the methanation process [7–9]. The Earth-abundant Ni-based catalysts have long been the top option for industrial applications and methanation process [10]. The Ni active metal is only one of several variables that affect the catalytic activity at temperatures below 400 ℃; other variables include supports, promoters, preparation conditions, reduction, and activation. In order to create highly dispersed Ni-based catalysts, oxide supports with a high specific surface area, such as Al_2O_3, SiO_2-Al_2O_3, and zeolites, are frequently used. Hotspots may form in the catalytic bed as a result of the exothermic nature of the reaction, which may result in the thermal aggregation of metallic Ni active sites and the catalysts become less stable. In order to solve these issues, well-defined crystalline structures are required to stabilize Ni active sites [11]. In this context, layered double hydroxide materials (LDH) were used as precursors to prepare our catalysts, which have been recently highlighted as promising candidates for CO_2 methanation catalysts [12–14]. The LDH has the general formula: $[M^{2+}_{1-x}\ M^{3+}_{x}\ (OH)_2](A^{n-})_{x/n}.mH_2O$, where M is a metal and A is an anion [15]. They consist of multiple positively-charged lamellar layers of combined divalent (Ni^{2+}, Mg^{2+}, etc.) and trivalent (Al^{3+}, etc.) metal cations surrounded by hydroxide ions and intercalated with anions such as CO_3^{2-} that serve as compensation charges and H_2O [16]. Catalyst materials such as LDH with characteristics having variable composition, adjustable acid-base properties, high surface area and dispersion, low crystallite size, and high stability and adsorption capacity are highly desirable [17,18]. Generally, LDH is synthesized by the traditional co-precipitation approach, which requires a long maturation phase [19]. Several new synthesis techniques have been invented to improve LDH texture, structural characteristics, and synthesis duration. Among these techniques, ultrasound irradiations have been used during the co-precipitation method [20–23]. Recently, ultrasonic irradiations have been used during the co-precipitation method. It can be utilized during the maturation phase [24,25] or in the early stages of co-precipitation in place of magnetic stirring [26]. On one hand, the acoustic cavitation induced by ultrasound technology leads to better particle dispersion, characterized by smaller sizes, a narrower particle size distribution, and an increased specific surface area as well as an increase in the number and strength of active basic sites, ultimately enhancing catalytic activity, selectivity, and stability [27–29]. On the other hand, the morphology of the materials can be strongly influenced by the duration of ultrasound exposure, density power, mode, amplitude, and frequency as well as the ultrasound apparatus [23,30,31]. Moreover, regarding the effect of ultrasound conditions, Kalawoun et al. [32] studied the effect of power density, and irradiation time during precipitation to evaluate the effect of acoustic cavitation on the incorporation of La atoms into LDH structure. They found that at a power density of 360 $W.L^{-1}$, applied successively to the precipitation step and the aging step, at room temperature and in 45 minutes, it was possible to obtain pure hydrotalcite phase and optimize the textural parameters of the materials (reduction of average crystallite, increase of specific surface areas, homogeneous dispersion and better insertion of La). Moreover, Yadav et al. [33] indicated that during the MnFe LDH synthesis using an ultrasonic homogenizer, the sonication time (20–80 min) and percentage of amplitude of power input (50–100 %) have significantly affected the structural, cationic distribution and physical property of the obtained material. They showed that the crystallite size of $NiFe_2O_4$ spinel ferrite increases from 1.8 to 22.1 nm by increasing the sonication time from 20 to 80 min and it increases from 19.3 to 25.5 nm by increasing the amplitude of power input from 50 % to 100 %. In addition, Munonde et al. [34] studied the impact of sonication time (3–20 min) and amplitude (50–90 %) in NiFe LDH synthesis in alkaline media using tip sonication. They found that by increasing the time and the amplitude, the interlayer spacing of the LDH structure decreases.

In this work, we have synthesized a series of LDH-type materials based on Ni active phase, basic magnesium, and stable alumina by the ultrasound-assisted co-precipitation method with different irradiation power densities (90, 180, 270, and 360 $W{\cdot}L^{-1}$). These catalysts were compared with the same catalyst prepared by the traditional (non-ultrasound-assisted) coprecipitation method. Unlike other studies that focus on the effect of ultrasonic frequency, time, and amplitude, the goal of this study is to investigate the influence of the ultrasonic power density in the ultrasound-assisted synthesis of Ni-based LDH catalysts for CO_2 methanation, a question that has not been addressed before on these types of materials and in the context of CO_2 methanation. Furthermore, this paper thoroughly examines the specific conditions employed in the ultrasound method, including ultrasonic power density, frequency, time, and mode. These factors can greatly influence the synthesis outcomes, thereby impacting catalytic performances and allowing the comparison of the obtained results with future studies.

2. Experimental section

2.1. Catalyst preparation

Co-precipitation and ultrasound-assisted co-precipitation methods were used to synthesize nickel, magnesium, and aluminum based-LDH precursors. The co-precipitation method (Cp) is thoroughly described in previous studies [35–37]. The solution containing the desired metal salts ($Ni(NO_3)_2.6\ H_2O$ (Alfa Aesar, purity 98 %), $Mg(NO_3)_2.6\ H_2O$ (ACROS ORGANICS, purity 99 %), $Al(NO_3)_3.9H_2O$ (Alfa Aesar, purity 98 %)) is added dropwise to deionized water with Na_2CO_3 (1 $mol{\cdot}L^{-1}$, ACROS ORGANICS, purity 99,5 %), whose pH is adjusted to 9 by a basic solution of NaOH (2 $mol{\cdot}L^{-1}$, ACROS ORGANICS, purity 98 %). After precipitation, the mixture was stirred for 18 h (maturation phase). The mixture was then filtered and the precipitate was washed with hot deionized water until a neutral pH was reached. This washing removes soluble ions (nitrate, Na^+, etc.). After 48 h in the oven at 60 ℃, the resulting dried solid was ground manually to powder in an agate mortar. The synthesis conditions were chosen according to the literature [38–41]. The sample prepared with this method was labeled as Ni Cp. The ultrasound-assisted co-precipitation method (Us) has the same steps as the co-precipitation at constant pH. The only difference is in the maturation step where the suspension was subjected for 30 min to ultrasonic irradiation (30 s on and 30 s off) instead of being stirred for 18 h. Four different power densities (90, 180, 270, and 360 $W{\cdot}L^{-1}$) were used in the irradiation while preparing four different samples. These samples were designated by Ni Us Z where the terminology Z is replaced hereafter by the power density used. The apparatus used in this maturation step is neither an ultrasonic bath nor an immersion probe. It is equipped with an ultrasonic pipe of 700 mL fitted with eight ultrasonic transducers at 22 kHz, each with a maximum power of 50 W. The device is driven by a Nextgen frequency generator (SinapTec ultrasonic technology) (see supplementary material). It should be noted that in our preparations, we took a molar ratio M(II)/M(III) = 3. In all samples, Ni content was 10 wt%. The resulting LDH were calcined under air (33 $mL{\cdot}min^{-1}$) at 800 ℃ for 4 h with a temperature rise of 2 $℃{\cdot}min^{-1}$, and were reduced at 800 ℃ under pure hydrogen (20 $mL{\cdot}min^{-1}$) for 2 h with a temperature rise of 5 $℃{\cdot}min^{-1}$. In the following of this article, the ending "LDH" is given for the dried samples, while the ending "calc" means that samples are calcined and the ending "red" designates reduced samples.

2.2. Characterization

The XRD investigations were carried out at room temperature using a BRÜKER D8 diffractometer. This diffractometer was operated with a LynxEye detector, a rotating sample holder (to prevent preferential orientations), and a copper anticathode generating K alpha radiation and operated at 40 kV and 40 mA. The standard acquisition parameters are an angle range in 2θ of 5–80 °, a measurement step size of 0.02 °, and an integration duration of 2 s. The diffractograms are compared to those

of reference compounds in the database of the "Joint Committee on Powder Diffraction Standards (JCPDS) database created by the International Center for Diffraction Data (ICDD)" to determine the crystalline phases. The EVA software is used for this comparison.

On a NETZSCH STA 409, differential thermal and thermogravimetric analysis (DTA/TG) was performed, with 10 mg for each sample, starting at room temperature and continuing up to 1000 °C (temperature rise of 5 °C·min^{-1}) with an airflow of 100 mL.min^{-1}. The obtained results are processed using the program "Universal analysis."

Using an Agilent 5100 SVDV spectrometer and inductively-coupled plasma optical emission spectroscopy (ICP-OES), the real Ni, Mg, and Al, weight contents of the produced materials were determined. The typical mineralization of the samples was as follows. 50 mg of powder was dissolved in 50 mL of ultrapure water after being digested for 4–6 hours at 80–90 °C with 1 mL of HNO_3 (65 % Normatom). Finally, 1 mL of the latter solution was diluted to a final volume of 10 mL by adding HNO_3 (2 %). Three duplicates of each analysis were carried out. To track instrument and digestive process contamination, blanks were also examined. Standards for calibration and quality control (drift, repeatability, and accuracy) were created from multi- and single-element standards (SCP Science). The average of the data collected with three or four different wavelengths was used to determine each element's concentration.

Temperature programmed reduction (H_2-TPR) experiments were carried out in a Micromeritics Autochem II chemisorption analyzer. About 50 mg of calcined sample were deposited in a quartz tube and pretreated under an argon flow of high purity. This argon flow of 50 mL.min^{-1}, circulates under a temperature ranging from ambient to 150 °C with a rise of 5 °C·min^{-1}. This step allows the catalyst activation by eliminating water and adsorbed surface impurities. After that, it is heated to 900 °C with a rise of 5 °C·min^{-1} under a H_2 flow (5 % H_2 in Ar, 50 mL·min^{-1}) followed by naturally cooling down under an Ar flow.

H_2-chemisorption of catalysts, reduced at 800 ℃, was carried out on the AutoChem III 2930 (Micromeritics Instrument Corporation) to determine nickel metal dispersion. Prior to pulse H_2 chemisorption, the 800 ℃ reduced catalyst was pretreated in 5 % H_2/Ar at a temperature rise rate of 10 ℃·min^{-1} up to 500 ℃, and held at 500 ℃ for 1 h. The sample was then purged and cooled to 35 ℃ in Ar flow. Pulse H_2 chemisorption was performed at 35 ℃ using 5 % H_2/Ar and repeated 10 times to obtain the saturated peak.

On a Micromeritics 3Flex version 5.03 instrument, textural analysis was carried out. The pre-treatment is performed at 350 °C for 4 hours under vacuum (continuous draft). The Brunauer-Emmett-Teller (BET) method is used to determine the specific surface area. Pore size distribution and volume were determined using the Barrett-Joyner-Halenda (BJH) method.

The XPS analyses were carried out with a SSX 100/206 photoelectron spectrometer from Surface Science Instruments (USA) equipped with a monochromatized micro focused Al X-ray source (powered at 20 mA and 10 kV). The samples powder pressed in small stainless-steel troughs of 4 mm diameter were placed on an aluminum conductive carousel. The pressure in the analysis chamber was around 10^{-6} Pa. The angle between the surface normal and the axis of the analyzer lens was 55°. The analyzed area was approximately 1.4 mm^2 and the pass energy was set at 150 eV. In these conditions, the full width measured at half maximum (FWHM) of the Au 4 $f_{7/2}$ peak for a clean gold standard sample was about 1.6 eV. A flood gun set at 8 eV and a Ni grid placed 3 mm above the sample surface were used for charge stabilization. The following sequence of spectra was recorded: survey spectrum, C 1 s, O 1 s, Ni 2p, Fe 2p, Mg 2 s, Mg 2p and C 1 s again to check the stability of charge compensation with time. The C-(C,H) component of the C1s peak of carbon has been fixed to 284.8 eV to set the binding energy scale. Data treatment was performed with the CasaXPS program (Casa Software Ltd, UK). Some spectra were decomposed with the least squares fitting routine provided by the software with a Gaussian/Lorentzian (85/15) product function and after subtraction of a non-linear baseline. Molar fractions were calculated using peak areas normalized based on acquisition parameters and sensitivity factors provided by the manufacturer.

Transmission electron microscopy (TEM) analyses were performed using a JEOL 2100Plus UHR microscope operating at 200 kV. The sample powder was ultrasonicated in ethanol and one drop of the resulting suspension was deposited on a copper grid coated with carbon film. For each sample, the mean surface diameters ($d=(n_i d_i^3)/(n_i d_i^2)$ with n_i: number of particles of diameter (d_i)) were determined by measuring at least 800 particles from TEM images. Scanning transmission electron microscopy (STEM) images were acquired using a high-angle annular dark-field (HAADF) detector. The image contrast in this mode is strongly correlated to the atomic number: heavier elements contribute to brighter contrast. Analytical investigation was performed with an energy-dispersive X-ray spectrometer (EDX) attached to the microscope column.

CO_2-TPD studies were carried out utilizing a CATLAB apparatus from Hiden Analytical outfitted with a QGA mass spectrometer for gas analysis to assess the basicity of the produced catalysts. 60 mg of the sample was positioned in a quartz microreactor and preheated under 50 mL·min^{-1} He flow (500 ℃ for 1 hour). The samples were cooled and subjected to 50 mL·min^{-1} 15 % CO_2 in He flow (50 ℃ for 1.5 hours). The catalysts were then purged for three hours with 50 mL·min^{-1} and then heated to 800 °C (5 °C·min^{-1}) to desorb the carbon dioxide. The amounts of desorbed CO_2 were obtained by integration of the desorption profiles and referenced to the signals calibrated for known volumes of the analyzed gases.

2.3. Catalytic test

For each catalytic test, the catalyst powders are sieved to obtain particle sizes between 355 and 500 μm. In addition, these tests are carried out using 150 mg of catalyst diluted with SiC to have an identical gas hourly space velocity (GHSV) of 6000 h^{-1}, regardless of the catalytic material used [42]. Prior to the evaluation of catalytic performance, the samples were reduced at 800 °C (5 °C.min^{-1}) for 2 h under a pure hydrogen flow of 20 mL·min^{-1}. The catalytic test was conducted with a fixed-bed reactor under atmospheric pressure and fed with a gas mixture of $CO_2/H_2/N_2$ with respective volume ratios 10/40/50 and a total flow rate of 100 mL·min^{-1}. The catalytic tests are performed at temperatures of 100, 150, 200, 220, 240, 260, 280, 300, 320, 340, 360, 380, and 400 °C with a rise of 5 °C·min^{-1}. At each temperature, the sample was kept for 30 min. Each test was performed three times, and the results for each catalyst did not vary by more than 1 %. The stability test was performed at 350 ℃ for 100 h under the same conditions. The composition of outlet gas (CO_2, CO, H_2 and CH_4) was analyzed by a Compaq gas chromatography system from Global Analyser. There are two analytical channels. The CO_2 gas is separated using the RTQ bond column, while the H_2, CO, and CH_4 gases are separated using the Molsieve 4 A column. These compounds are detected using thermal conductivity detectors (TCD1 and TCD2). The CO_2 conversion and the CH_4 and CO selectivity are defined as:

$$\text{Conversion of CO2 : XCO2(\%)} = \frac{nCO2in - nCO2out}{\text{nCO2in}} \times 100 \quad (2)$$

$$\text{Selectivity of methane : SCH4(\%)} = \frac{\text{nCH4formed}}{\text{nCO2in} - \text{nCO2out}} \times 100 \quad (3)$$

$$\text{Selectivity of CO : SCO(\%)} = \frac{\text{nCO formed}}{\text{nCO2in} - \text{nCO2out}} \times 100 \quad (4)$$

nCO_2in and nCO_2out are respectively the number of moles of CO_2 at the inlet and the outlet of the reactor, nCH_4 formed and nCO formed are respectively the number of moles of CH_4 and CO obtained.

The turnover frequency (TOF) values towards CO_2 were calculated according to Eq. 5 [43].

$$\mathrm{TOF}\left(\mathrm{sec}^{-1}\right) = \frac{[CO_2]_{in} \times X_{CO_2} \times M}{m \times L \times A\%} \quad (5)$$

where CO_2 (in) represents the molar flow rates of CO_2 at the inlet ($mol{\cdot}s^{-1}$); XCO_2 represents the conversion of CO_2; m represents the weight of catalyst (g); L represents the loading of Ni in the catalyst determined by ICP (taking into account the degree of nickel reduction determined by H_2-TPR); M represents the molar weight of Ni ($g{\cdot}mol^{-1}$); A% represents the accessibility of Ni, which is determined by H_2-chemisorption.

3. Results and discussion

3.1. Characterization of the dried LDH samples

LDH samples were characterized after synthesis by X-ray diffraction and thermal analysis. X-ray diffractograms are presented in the supplementary material and confirm that the LDH structure was obtained when ultrasound was used in the maturation phase while reducing synthesis time. The cell parameters "a" and "c" determined from the X-ray diffractograms corresponding respectively to the average cation-cation distance in the layers and the thickness of the hydroxide layers [44] were calculated for all samples and presented in the supplementary material. "a" does not change when changing the power density, while "c" decreases when using ultrasound and increasing the density power. Furthermore, LDH crystallite size was calculated using the Debye-Scherrer equation, taking the first most intense peak for calculation. These results are presented in Table S1 in the supplementary material. The crystallite size of the LDH prepared by ultrasound-assisted coprecipitation is smaller, regardless of the power density used, than that of the sample prepared by the conventional method. The use of ultrasound appears to increase the nucleation rate relative to the crystal growth rate [26,32]. Moreover, the LDH crystallite size increases from 54 to 59 Å while increasing the power density from 90 to 360 $W{\cdot}L^{-1}$. These results may be due to local overheating of the suspension when the power density increases during ultrasonic treatment [45].

Finally, it is interesting to mention that at 800 °C, the LDH structure is destroyed in all our samples as shown by thermal analysis (see supplementary material). Moreover, from these temperatures, the recorded mass loss is negligible. Hence the choice of this temperature for the treatment of the synthesized dried solids.

3.2. Characterization of the calcined and reduced samples

Fig. 1 shows the X-ray diffractograms of Ni Cp and Ni Us Z calcined under air ($33\ mL{\cdot}min^{-1}$) at 800 °C for 4 h (a), and reduced at 800 °C under pure hydrogen ($20\ mL{\cdot}min^{-1}$) for 2 h (b).

The diffraction peaks at 37 °, 43 °, and 62 ° in Fig. 1(a) are ascribed to simple oxides MgO (JCPDS N°43–1022), solid solutions $MgNiO_2$ (JCPDS N°24–0712), and spinels $NiAl_2O_4$ (JCPDS N°65–3102) and $MgAl_2O_4$ (JCPDS N°75–0713). In general, calcination at high temperatures (800 °C) promotes the formation of spinel-like solid solutions of Ni^{2+}–Al^{3+} and Mg^{2+}–Al^{3+} [46,47]. These phases are particularly evident on the calcined sample, which was analyzed prior to reduction. Some oxide phases are also detected on the reduced material (Fig. 1(b)), demonstrating that not all oxides were reduced following H_2-pretreatment. The metallic Ni (JCPDS N° 04–0850) lines appear at $2\theta = 44$ °, 52 °, and 76 °. Moreover, using ultrasound irradiations in the maturation phase and increasing its output density power does not affect the crystalline phases.

The specific surface area, the pore diameters and volumes, and the experimental metal loading determined by ICP-OES analysis of the different calcined solids are grouped in Table 1.

The values of the experimental metal loading from ICP analysis (Table 1) are very close to the desired content in the catalysts. All samples revealed a nickel content around 8.5–9.5 wt%. The calculated M^{2+}/M^{3+} atomic ratios were reasonably close to the nominal ones presented in parentheses in the table, indicating that LDH composition can be easily controlled as previously reported [48].

N_2 adsorption and desorption isotherms recorded at – 196 °C for the calcined Ni Cp and Ni Us Z materials are presented in the supplementary material. For all solids, they are of type IVa, according to the IUPAC

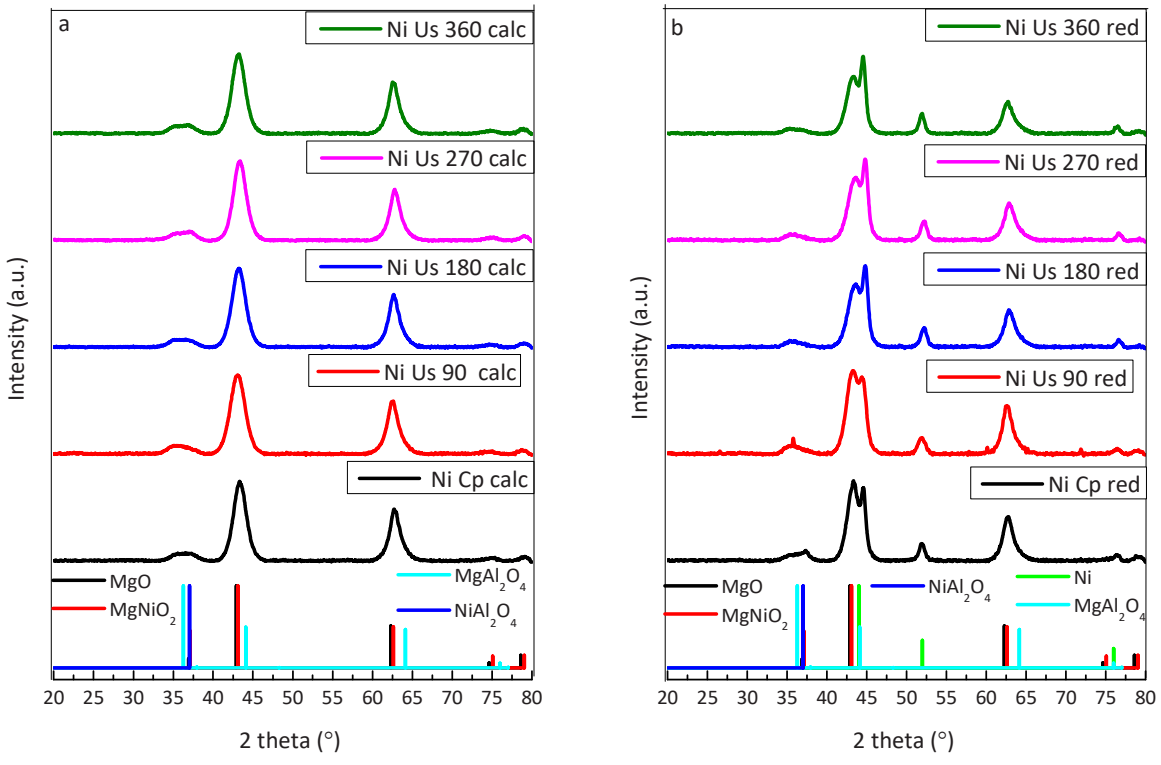

Fig. 1. : X-ray diffraction patterns of the calcined samples Ni Cp and Ni Us z (a), and reduced samples Ni Cp and Ni Us z (b).

Table 1
Specific surface area, pore diameter, pore volume, and experimental metal loading of the calcined samples.

Sample	$S_{BET}^{[a]}$ ($m^2 \cdot g^{-1}$)	$S\mu^{[b]}$ ($m^2 \cdot g^{-1}$)	$S_{meso}^{[c]}$ ($m^2 \cdot g^{-1}$)	$V_p^{[d]}$ ($cm^3 \cdot g^{-1}$)	$d_p^{[d]}$ (nm)	$Ni^{[e]}$ (wt%)	$Mg^{[e]}$ (wt%)	$Al^{[e]}$ (wt%)	M^{2+}/M^{3+}
Ni Cp calc	202	36.49	165.51	0.44	9.82	9.01	28.75	12.91	2.92 (3.0)[f]
Ni Us 90 calc	232	23.47	208.53	0.74	11.15	9.28	29.58	13.56	2.87 (3.0)
Ni Us 180 calc	233	21.58	211.42	1.09	14.47	8.75	28.59	12.81	2.91 (3.0)
Ni Us 270 calc	233	18.72	214.28	1.2	15.09	9.28	30.3	13.62	2.91 (3.0)
Ni Us 360 calc	200	19.68	180.32	0.64	10.33	9.53	28.62	13.68	2.79 (3.0)

[a] determined by BET method. [b] determined by the t-plot method. [c] calculated by $S_{meso}=S_{BET}-S_{\mu}$. [d] determined by BJH method. [e] determined from ICP-OES analysis. [f] calculated from nominal values.

classification [49]. This type corresponds to mesoporous materials. The hysteresis loops of the various solids are of type H3, characteristic of uniform pore size [50,51]. The pore size distribution (see supplementary material) shows the uniformity of the pore size diameter.

Comparing the specific surface area, pore diameter, and pore volume of Ni Cp calc and Ni Us Z calc (Table 1), an increase is noted when ultrasound is used in the maturation phase, regardless of the power density used, except for the specific surface area of Ni Us 360 calc, which is similar to that of Ni Cp calc. In the Ni Us Z calc series, a decrease in specific surface area, pore volume, and pore diameter is observed for a power density of 360 $W \cdot L^{-1}$. It seems that beyond 270 $W \cdot L^{-1}$, the use of ultrasound destroys the porous structure, leading to a decrease in specific surface area, pore volume, and pore diameter. The same effect was obtained by Shamskar et al. [52], who synthesized NiO-Al_2O_3 using the ultrasound-assisted co-precipitation method. It seems that the bubbles generated during ultrasonic irradiation collapse locally and forcefully after several acoustic cycles in the irradiation solution, producing high temperatures and pressures thus increasing the probability of destroying the porous structure.

Furthermore, the specific surface area of micropores determined by the t-plot method is higher for the sample prepared without ultrasound than for all samples prepared with ultrasound, regardless of the power density (Table 1). These results show that ultrasound can introduce more mesoporosity than microporosity into the material, which explains the increase of pore volume and pore diameter with increasing power density from 90 to 270 $W \cdot L^{-1}$ while the specific surface area remains the same. These findings correlate with those of Zhuang et al. [53] who synthesized a series of zeolites with and without ultrasound while changing the sonication time, and showed that when using ultrasound, the mesopore volume increases and the micropore one decreases.

The H_2-TPR profiles of Ni Cp calc and Ni Us Z calc samples are shown in Fig. 2.

First of all, for all the samples, nickel oxide species are reduced at high temperatures (between 788 and 820 °C) as a result of spinel formation [54], as suggested by the XRD study. Due to the production of spinel, a characteristic event undergone by catalysts formed from LDH-like precursors, the reduction temperatures of NiMgAl mixed oxides are high. This suggests that nickel ions in the solid matrix have strong interactions, making it challenging to reduce nickel oxide species at lower temperatures. This difficulty in nickel species reduction renders it more resistant to sintering, resulting in the ability to maintain a high dispersion and finite size of Ni^0 [55]. The reduction temperature for the Ni Us 90 calc and Ni Us 180 calc samples is lower than for the Ni Cp calc sample. Moreover, it is higher for Ni Us 270 calc and Ni Us 360 calc than for the Ni Cp calc sample. It should be noted that under our TPR conditions, aluminum and magnesium oxides are not reduced [56]. The theoretical value for H_2 consumption is close to the experimental values (Table 2). These values are typically lower than their theoretical counterparts. These results indicate that not all species have been converted into metallic ones which may be due to the presence of spinel oxides, as revealed by XRD, which are difficult to reduce. The highest experimental value of the amount of hydrogen consumed is obtained for the Ni Us 90 calc sample. This indicates that nearly all of the nickel in this sample has been reduced. This might occur since a large dispersion of the active phase makes it more accessible to the reducing agent. These results are very important, especially for the industry, because a minimal power density of 90 $W \cdot L^{-1}$ is sufficient to obtain a good distribution and reducibility of nickel compared to other power densities while saving energy consumption by a factor of 3 compared to the highest power density used.

High resolution TEM (HRTEM) was used to examine the Ni particle crystal structure. Fig. 3 shows an image of individual particle of Ni Us 90

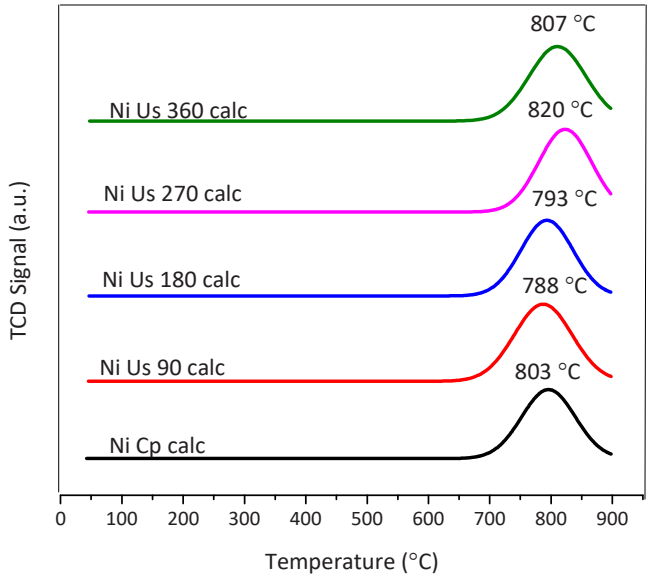

Fig. 2. : H_2-temperature programmed reduction (TPR) profiles for Ni Cp and Ni Us Z calc.

Table 2
Experimental and theoretical hydrogen consumption and degree of reduction of nickel in Ni Cp and Ni Us Z materials.

Sample	Experimental hydrogen consumption (10^3 µmol.g^{-1})	Theoretical hydrogen consumption (10^3 µmol.g^{-1})[a]	Degree of reduction[b] (%)
Ni Cp calc	1.33	1.62	82
Ni Us 90 calc	1.68	1.68	100
Ni Us 180 calc	1.43	1.58	91
Ni Us 270 calc	1.56	1.68	93
Ni Us 360 calc	1.51	1.73	87

[a] calculated using the experimental nickel loading determined by ICP.
[b] percentage of reducible species that have actually been reduced.

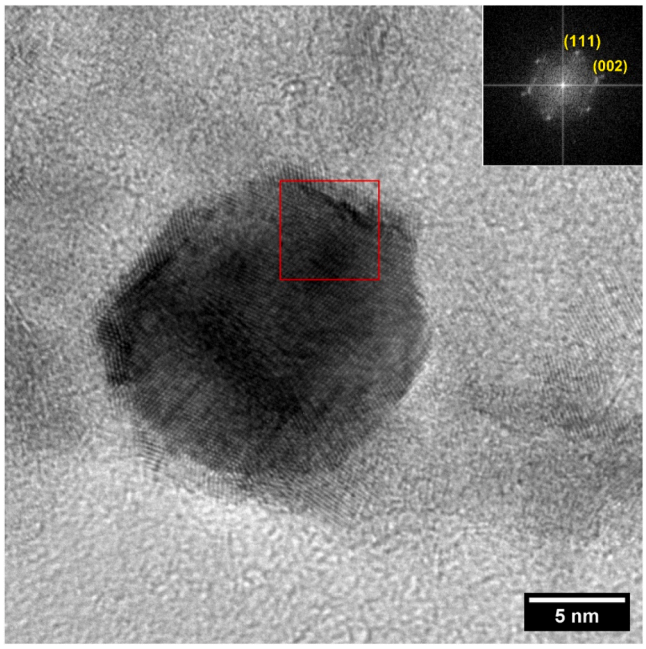

Fig. 3. : HRTEM image of a nickel particle of the Ni Us 90 red sample. The inset shows the FFT of the red squared area.

red sample as an example. Fast Fourier Transform (FFT) on the red-framed region reveals the distinctive cubic phase structure for metallic nickel.

Fig. 4 displays representative TEM-measured particle size distributions for the reduced samples. In the case of the Ni Us 90 red catalyst (Fig. 4(b)), a homogeneous distribution of nickel particles is observed with an average of around 8.2 nm, while it is around 13.5 nm for the Ni Us 180 red (Fig. 4(c)), 14.1 nm for the Ni Us 270 red (Fig. 4(d)) and around 15.8 nm for Ni Us 360 red (Fig. 4(e)). For the sample prepared without ultrasound, the average diameter of the nickel particle is 13.1 nm (Fig. 4(a)). This study demonstrates that all applied power densities permit a particle size reduction compared to a conventional co-precipitation sample. Among all power densities, the sample prepared with 90 $W{\cdot}L^{-1}$, has the smallest particles. This may be due to the fact that beyond an optimal power, the use of ultrasound increases the probability of agglomerate formation, leading to an increase of the size of the particles [52,57].

Nickel dispersion estimated by TEM and determined by H_2-chemisorption shows the same trend (Table 3). But the former shows higher values than the latter. These results are in line with those obtained by Daoura et al. [59]. This underestimation of nickel dispersion determined by H_2-chemisorption can be attributed to hydrogen accessibility to nickel sites present only at the surface. Note that in the TEM, the nickel dispersion was estimated taking into account particles present in the sample (on the surface and in the bulk). Furthermore, Ni dispersion determined by H_2-chemisorption was increased from 6.7 % to 8.1 % when 90 $W{\cdot}L^{-1}$ was used during the ultrasound irradiation (Table 3). These results confirm that the sample with the smallest nickel particle size exhibits the greatest dispersion, as already shown by Razzaq et al. [60]. The application of ultrasound in the maturation phase of LDH causes acoustic cavitation within the medium. This generates numerous micro-bubbles that violently collapse, resulting in the release of significant amounts of energy [61]. In this distinctive environment, ultrasonic energy's results in the intense shear, mixing, and distribution of the metals present in the solution. It also triggers particle fragmentation through inter-particle collisions that effectively break apart aggregates and reveal fresh and exposed surfaces [62,63]. On the other hand, as ultrasonic density power increases, nickel dispersion decreases. This result confirms that this may be since 90 $W{\cdot}L^{-1}$ is an optimal density power to give the necessary energy to enable better dispersion, whereas a higher power density allows to increase the energy and temperature of the solution, thus increasing the probability of forming aggregates as revealed by XRD.

Fig. 5 illustrates the TPD-CO_2 profiles of the reduced Ni Cp and Ni Us Z samples.

A single peak was observed in the 100–300 °C temperature range and attributed to weak basic sites [64]. At low temperatures, CO_2 desorption is linked to CO_2 released by bidentate carbonates formed on weak basic sites [65]. These weak sites are characteristic of CO_2 molecules interacting with surface hydroxyl groups and Mg^{2+}-O^{2-} and Al^{3+}-O^{2-} pairs [47,66]. The samples contain a total amount of basic sites ranging from 77 to 94 $\mu mol{\cdot}g^{-1}$ (Table 3). These samples do not contain strong basic sites attributable to CO_2 strongly adsorbed on the surface [67,68]. It is worth mentioning that Ni Us 90 red shows the highest amount of basic sites. This could be explained by the fact that using a power density of 90 $W{\cdot}L^{-1}$ leads to a greater number of irregularities on the surface, resulting in a greater number of exposed HO^- sites [27]. These results show that ultrasonic irradiation power densities above 90 $W{\cdot}L^{-1}$ do not increase the basicity of materials.

The X-ray photoelectron spectroscopy (XPS) spectra for the reduced Ni Cp and Ni Us z samples is shown in Fig. 6.

They confirmed the presence of both Ni^{2+} and Ni^0 on the sample surface. The high-resolution Ni 2p3/2 spectra (Fig. 6) shows three major peaks. The lower energy components at 852.3 eV is attributed to metallic Ni species, while the component at 855.6 eV is assigned to Ni^{2+} and the one at 861.4 eV is a satellite peak from Ni^{2+} [69–71]. The XPS measurement findings are summarized in Table 4.

The Ni 2p3/2 for all catalysts is accompanied by a satellite peak at 861–863 eV, which is consistent with the presence of Ni^{2+} [72]. The ΔE_{sat} values in Table 4 show that these peaks are typically 4.8–6 eV higher than the primary Ni 2p3/2 peak [73]. Since XPS analysis is surface sensitive, the variations in binding energies suggested that the electronic state of the Ni species on the surface has been changed [62], in this case as a result of the use of ultrasound during the catalysts' production and with changing its power density. The extent of the metal-support interaction between the Ni phase and the support was also changed as revealed by a change in binding energy [74]. The samples prepared with a density power of 90 and 180 $W{\cdot}L^{-1}$ have a binding energy of Ni^{2+} a little bit lower than those obtained for the samples prepared without ultrasound and with ultrasound under 270 and 360 $W{\cdot}L^{-1}$. In this instance, other researchers have noted a shift to lower binding energies brought on by ultrasound compared with samples prepared without ultrasound [75]. This change in electron density may have an impact on the bonding of chemical intermediates to the active sites, as shown by the difference in reduction temperatures of nickel species determined by TPR. In particular, the shift in the reduction peak to lower temperature while using the power densities 90 and 180 $W{\cdot}L^{-1}$, further supports this idea of small deterioration in Ni-matrix interactions.

The CO_2 conversion over Ni Cp and Ni Us Z as a function of temperature is presented in Fig. 7.

Thermodynamics states that practically total CO_2 conversion is achievable at temperatures below 200 ℃, and that it declines with rising the temperature, as indicated by the dashed line, due to the coexistence of parallel processes, which produce undesirable side products, including carbon monoxide. At temperatures below 200 °C, the CO_2 conversion of all catalysts is negligible (Fig. 7(a)). The conversion of CO_2 increases with temperature. Although the CO_2 molecule is relatively stable and the methanation reaction is exothermic, the activation of this molecule requires a significant energy input due to its chemical inertia. This energy is delivered thermally. For all the catalysts an almost complete selectivity (99.9 %) at 350 ℃ towards methane was recorded which validates that changing the ultrasound power density does not affect the selectivity. First of all, comparing the CO_2 conversion at 350 °C of all catalysts (Fig. 7(a)) reveals that the sample prepared with

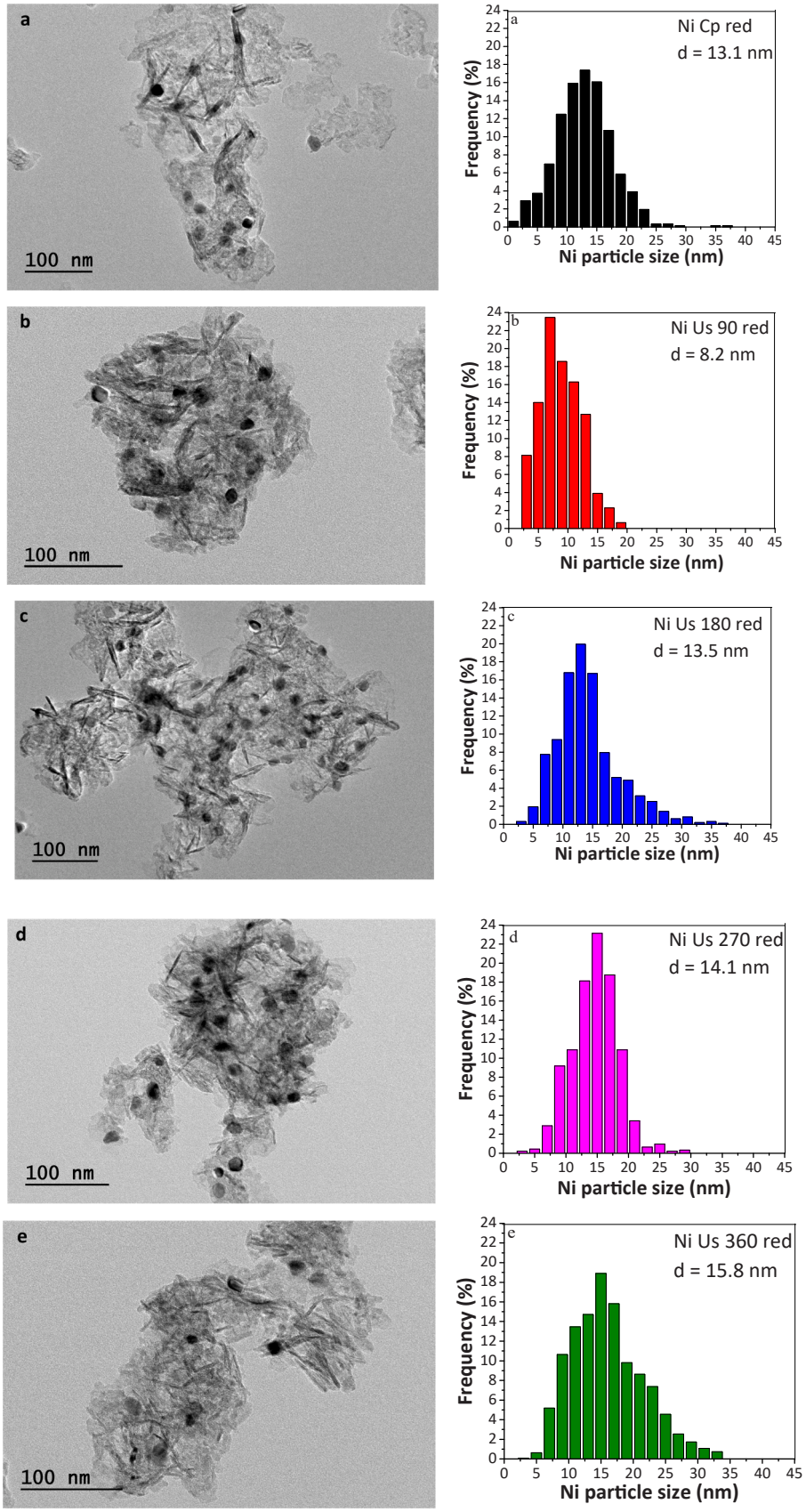

Fig. 4. : TEM micrographs and particle size distributions for (a) Ni Cp red, (b) Ni Us 90 red, (c) Ni Us 180 red, (d) Ni Us 270 red and (e) Ni Us 360 red.

Table 3
Ni particle size and dispersion and total amount of basic sites in reduced Ni Cp red and Ni Us Z red samples.

Sample	Ni particle size [a] (nm)	Ni dispersion [b] (%)	Ni accessibility [c] (%)	Total amount of basic sites [d] (μmol·g^{-1})
Ni Cp red	13.1	10.1	6.7	85
Ni Us 90 red	8.2	16.1	8.1	94
Ni Us 180 red	13.5	9.8	6.2	82
Ni Us 270 red	14.1	9.4	5.4	77
Ni Us 360 red	15.8	8.3	4.8	79

[a] Ni particle size determined by TEM analysis.
[b] Ni particle dispersion calculation based on Ni particle size. The calculation details can be found in the reference [58].
[c] Ni particle accessibility determined by H_2-chemisorption.
[d] Amount of CO_2 desorbed during TPD-CO_2.

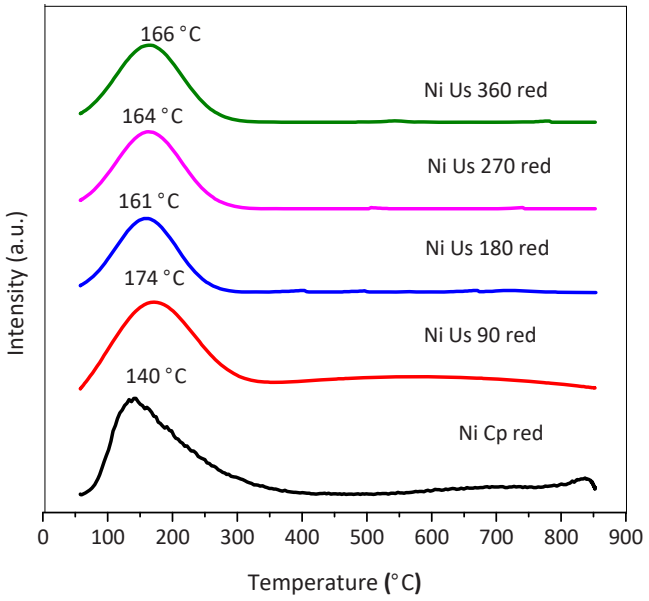

Fig. 5. TPD-CO_2 profiles of the reduced Ni Cp and Ni Us Z.

90 W·L^{-1} of power density has the highest CO_2 conversion, followed by the sample prepared without ultrasound irradiation and the samples prepared with 180 W·L^{-1}, 360 W·L^{-1}, and 270 W·L^{-1}. These results demonstrate that 90 W·L^{-1} of power density is adequate to achieve a high CO_2 conversion at 350 ℃. The XPS investigations show a shift to lower binding energies brought on by using 90 W·L^{-1} as power density compared with other samples prepared with different power densities and with samples prepared without ultrasound. This change in electron density may have an impact on the bonding of chemical intermediates to the active sites, as shown by the difference in reduction temperatures of nickel species determined by TPR. The sample Ni Us 90 shows that its nickel particles reduce at the lowest temperature among all other samples prepared by Cp Us and Cp. Furthermore, all nickel presented in Ni Us 90 is reduced (100 % reduction percentage according to Table 2). This can be related to the smaller nickel particle size (8.2 nm) obtained by TEM as well as the larger nickel particle distribution determined by H_2-chemisorption. Thus, a small particle size results in a better dispersion than larger particles, thus increasing catalytic activity. This is because larger Ni particles have less concentration of active sites due to low dispersion, resulting in poor catalytic activity [60,76]. In addition, Ni Us 90 has the highest amount of basic sites (94 μmol·g^{-1}) which is very important for capturing more the CO_2. It is for these reasons that Ni Us 90 shows the highest CO_2 conversion at low temperatures. Fig. 7(b) shows the stability test of Ni Us 90. The latter remains stable for 100 h under the stream with no deactivation, and the selectivity for methane remains higher than 99.5 %.

According to the literature [77–80], two commonly accepted pathways have been suggested for CO_2 methanation, the formate pathway also known as associative CO_2 methanation, and the CO pathway also known as dissociative CO_2 methanation. On our types of material and according to in situ DRIFTS measurements in the literature [6,81], the main CO_2 adsorption intermediates were carbonate-type species (1600–1000 cm^{-1}), which reacted with hydrogen and gradually disappeared into formate-type species, then methane. Therefore, CO_2 methanation follows the formate pathway.

The turnover frequency (TOF) values towards CO_2 (Fig. 8) were defined as the number of CO_2 molecules converted per surface metallic Ni active site per second [82]. The comparison of TOF values of the catalysts towards CO_2 conversion with a CO_2 conversion value of less than 15 % allows the potential effect of mass and heat transfer to be neglected [83,84]. Ni Us 90 exhibits the highest TOF value (0.066 s^{-1}) at 260 ℃ (Fig. 8), implying its higher intrinsic activity in CO_2 methanation. This is because an increase in dispersion and a decrease in particle size are promising in catalysis, as more active sites are then accessible to the reactants [62]. Furthermore, by increasing the density power, the nickel particle size decreases, which reduces nickel dispersion and therefore TOF. In addition, in order to verify the presence of carbon and particle sintering, XRD and thermal analysis were carried out on the samples after catalytic testing. The results of the thermal analysis (see supplementary material) showed only one exothermic peak attributed to the oxidation of metallic nickel. Furthermore, the results of the XRD analysis (see supplementary material) showed that the size of the nickel crystals exhibited the same trend before and after the catalytic test. Thus, we can conclude that for all the samples Ni Cp and Ni Us Z, there is no presence of carbon or particle sintering.

The catalyst reported in the present study is more effective than most of the already reported catalysts based on LDH, with a CO_2 conversion of approximately 80 % and a CH_4 selectivity of 99.9 %. In our previous study [85], we synthesized 10 % of Ni impregnated on NiMg mixed oxides issued from LDH precursors. This catalyst showed 35 % of CO_2 conversion and 99.9 % of methane selectivity at 350 ℃. With the same amount of nickel, the catalyst 10 %Ni-LDH prepared by Wierzbicki et al. [86] was evaluated with a GHSV (12000 h^{-1}), different than that employed in our study (6000 h^{-1}), and had a CO_2 conversion of approximately 62 %. On the other hand, with a higher amount of nickel, the 59 %Ni-LDH catalyst prepared by Bette et al. [87] converted 74 % of the CO_2 at 350 ℃, and the 33 %Ni-LDH catalyst prepared by Dias et al. [88] and the 20 %Ni-LDH catalyst prepared by Wierzbicki et al. [89] converted 70 % of the CO_2 at 350 ℃ with different GHSV. This succinct summary was used to compare the Ni Us 90 performance to studies that were published in the literature. Considering essential factors like metal loading and contact time, our Ni Us 90 catalyst prepared by ultrasound-assisted co-precipitation method appears to be particularly active in the CO_2 methanation reaction.

4. Conclusion

Nickel-based LDH were successfully synthesized using the ultrasound-assisted co-precipitation method.

Unlike other studies that focus on the effect of ultrasonic frequency, and time, this paper investigates the influence of ultrasonic power density during the maturation phase. The resulting properties are compared to those obtained through the conventional co-precipitation method. Treating the solids with different ultrasonic power densities

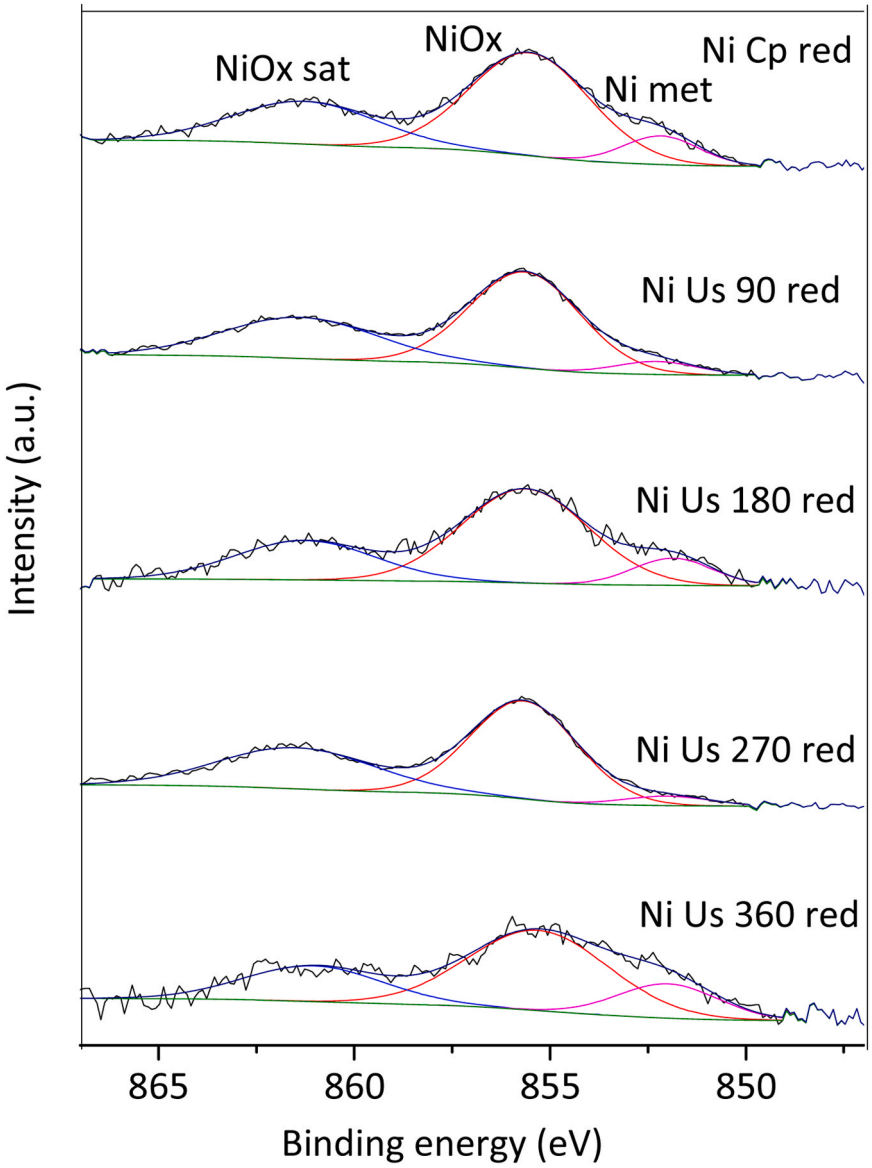

Fig. 6. : Ni 2p3/2 X-ray photoelectron spectroscopy (XPS) spectra.

Table 4
XPS analysis results for the reduced Ni Cp and Ni Us Z catalysts.

Samples	Ni 2 p3/2 (eV)	Ni 2 p3/2 satellite (eV)	ΔE sat [a] (eV)
Ni Cp red	855.74	861.3	5.6
Ni Us 90 red	855.64	861.4	5.8
Ni Us 180 red	855.66	861.5	5.8
Ni Us 270 red	856.15	861.1	4.8
Ni Us 360 red	856.01	861.2	5.2

[a] Separation between Ni 2p3/2 primary line and satellite.

affects the crystallite size of the dried LDH materials, and increasing the power density, the crystallite size increases, meaning that the probability of agglomerate formation increases. In addition, ultrasound affects the porosity of the materials, as their application in the maturation phase increases mesoporosity more than microporosity. Furthermore, modifying density powers affects nickel particle size and dispersion. Precisely by increasing density power, nickel particle size increases, thus reducing dispersion.

The catalyst synthesized by the ultrasound-assisted co-precipitation method with 90 $W{\cdot}L^{-1}$ shows a CO_2 conversion of 80 % at 350 ℃. This is due to the smaller size of the highly distributed nickel particles with improved reducibility and the presence of higher amount and more basic sites. These results are very important, particularly for industry, as the ultrasound-assisted co-precipitation method reduces time from 18 hours to 30 min compared to conventional co-precipitation. In addition, Ni Us 90 prepared by the Us method with a power density of 90 $W{\cdot}L^{-1}$ remained stable for 100 hours under reaction conditions. This catalyst therefore offers great potential to be employed in the methanation process, while saving time and energy. It is important to mention that 90 $W{\cdot}L^{-1}$ is the lower limit density power that our available Us equipment made it possible to explore.

Formatting of funding sources

This research did not receive any specific grant from funding agencies in the public, commercial, or not-for-profit sectors.

CRediT authorship contribution statement

Michel OBEID: Writing – original draft, Methodology, Data curation. **Christophe Poupin:** Writing – review & editing, Supervision,

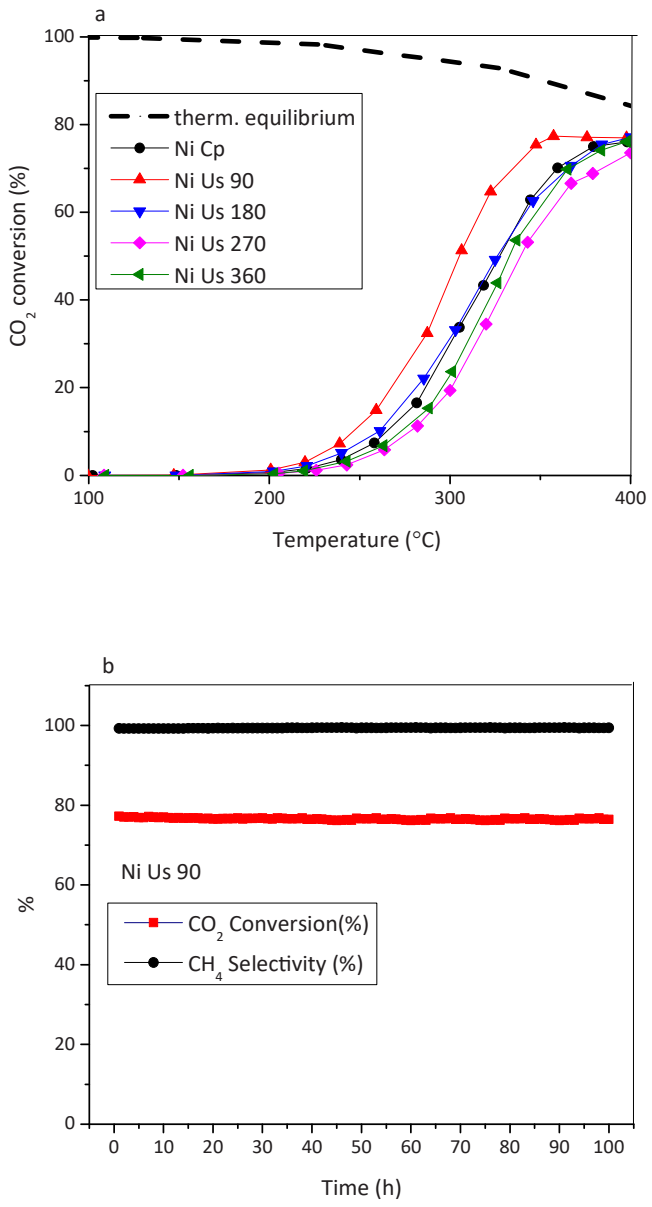

Fig. 7. (a) CO_2 conversion on Ni Cp and Ni Us Z samples (P = 1 atm, H_2/CO_2 = 4 and GHSV = 6000 h^{-1}), (b) long-term stability test over Ni Us 90 at 350 °C (P = 1 atm, H_2/CO_2 = 4 and GHSV = 6000 h^{-1}).

Methodology, Conceptualization. **Madona LABAKI:** Writing – review & editing, Supervision, Methodology, Conceptualization. **Sharad GUPTA:** Writing – review & editing. **Samer AOUAD:** Writing – review & editing. **François DELATTRE:** Writing – review & editing. **Ferdaous Ben Romdhane**: Writing - review & editing, Data curation. **François DEVRED:** Writing – review & editing, Data curation. **Eric M. GAIGNEAUX:** Writing – review & editing. **Josefine SCHNEE:** Writing – review & editing, Data curation. **Edmond ABI-AAD:** Supervision, Project administration, Conceptualization.

Declaration of Competing Interest

The authors declare the following financial interests/personal relationships which may be considered as potential competing interests: Michel Obeid reports financial support was provided by University of the Littoral Opal Coast Environmental Chemistry and Interactions with Living Organisms Research Unit. If there are other authors, they declare that they have no known competing financial interests or personal relationships that could have appeared to influence the work reported in this paper.

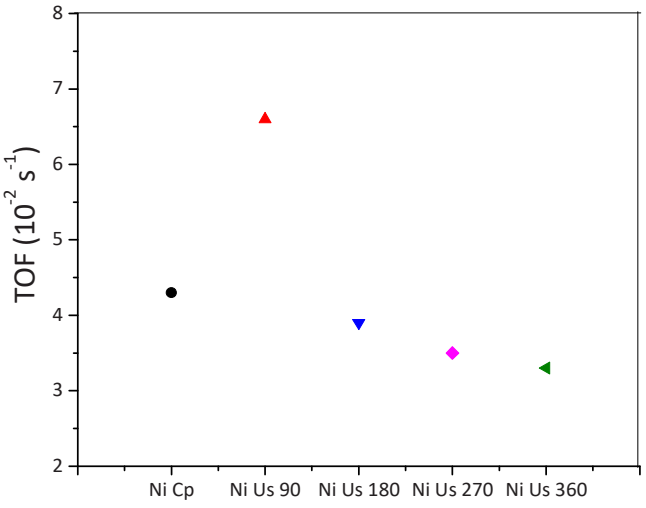

Fig. 8. Variation of TOF at 260 °C during CO_2 conversion of Ni Cp, and Ni Us z (P = 1 atm, H_2/CO_2 = 4 and GHSV = 6000 h^{-1}).

Data availability

Data will be made available on request.

Acknowledgment

The TEM microscopes are facilities of the Chemistry and Materials Federation of Paris-Centre (FCMat) and were funded by Sorbonne Université, CNRS, and Région Ile de France which are gratefully acknowledged.

Appendix A. Supporting information

Supplementary data associated with this article can be found in the online version at doi:10.1016/j.jece.2024.114059.

References

[1] M.H. Albadi, E.F. El-Saadany, Overview of wind power intermittency impacts on power systems, Electr. Power Syst. Res. 80 (2010) 627–632, https://doi.org/10.1016/j.epsr.2009.10.035.
[2] J. Nowotny, T. Bak, D. Chu, S. Fiechter, G.E. Murch, T.N. Veziroglu, Sustainable practices: solar hydrogen fuel and education program on sustainable energy systems, Int. J. Hydrog. Energy 39 (2014) 4151–4157, https://doi.org/10.1016/j.ijhydene.2013.12.114.
[3] P. Marocco, E.A. Morosanu, E. Giglio, D. Ferrero, C. Mebrahtu, A. Lanzini, S. Abate, S. Bensaid, S. Perathoner, M. Santarelli, R. Pirone, G. Centi, CO_2 methanation over Ni/Al hydrotalcite-derived catalyst: experimental characterization and kinetic study, Fuel 225 (2018) 230–242, https://doi.org/10.1016/j.fuel.2018.03.137.
[4] H. Muroyama, Y. Tsuda, T. Asakoshi, H. Masitah, T. Okanishi, T. Matsui, K. Eguchi, Carbon dioxide methanation over Ni catalysts supported on various metal oxides, J. Catal. 343 (2016) 178–184, https://doi.org/10.1016/j.jcat.2016.07.018.
[5] S. Rönsch, J. Schneider, S. Matthischke, M. Schlüter, M. Götz, J. Lefebvre, P. Prabhakaran, S. Bajohr, Review on methanation – from fundamentals to current projects, Fuel 166 (2015) 276–296, https://doi.org/10.1016/j.fuel.2015.10.111.
[6] X. Guo, D. Gao, H. He, A. Traitangwong, Promotion of CO_2 methanation at low temperature over hydrotalcite-derived catalysts-effect of the tunable metal species and basicity, Int. J. Hydrog. Energy 9 (2020) 193, https://doi.org/10.1016/j.ijhydene.2020.09.193.
[7] B. Miao, S.S.K. Ma, X. Wang, H. Su, S.H. Chan, Catalysis mechanisms of CO_2 and CO methanation, Catal. Sci. Technol. 6 (2016) 4048–4058, https://doi.org/10.1039/c6cy00478d.
[8] C. Vogt, M. Monai, G.J. Kramer, B.M. Weckhuysen, The renaissance of the Sabatier reaction and its applications on Earth and in space, Nat. Catal. 2 (2019) 188–197, https://doi.org/10.1038/s41929-019-0244-4.
[9] P. Frontera, A. Macario, M. Ferraro, P.L. Antonucci, Supported catalysts for CO_2 methanation: a review, Catalysts 7 (2017) 1–28, https://doi.org/10.3390/catal7020059.

[10] H.L. Huynh, Z. Yu, CO2 methanation on hydrotalcite-derived catalysts and structured reactors: a review, Energy Technol. 8 (2020), https://doi.org/10.1002/ente.201901475.
[11] W. Li, H. Wang, X. Jiang, J. Zhu, Z. Liu, X. Guo, C. Song, A short review of recent advances in CO_2 hydrogenation to hydrocarbons over heterogeneous catalysts, RSC Adv. 8 (2018) 7651–7669, https://doi.org/10.1039/c7ra13546g.
[12] C. Sun, K. Świrk, D. Wierzbicki, M. Motak, T. Grzybek, P. Da Costa, On the effect of yttrium promotion on Ni-layered double hydroxides-derived catalysts for hydrogenation of CO_2 to methane, Int. J. Hydrog. Energy 46 (2021) 12169–12179, https://doi.org/10.1016/j.ijhydene.2020.03.202.
[13] F. He, J. Zhuang, B. Lu, X. Liu, J. Zhang, F. Gu, M. Zhu, J. Xu, Z. Zhong, G. Xu, F. Su, Ni-based catalysts derived from Ni-Zr-Al ternary hydrotalcites show outstanding catalytic properties for low-temperature CO_2 methanation, Appl. Catal. B Environ. 293 (2021) 120218, https://doi.org/10.1016/j.apcatb.2021.120218.
[14] D. Wierzbicki, R. Baran, R. Dębek, M. Motak, M.E. Gálvez, T. Grzybek, P. Da Costa, P. Glatzel, Examination of the influence of La promotion on Ni state in hydrotalcite-derived catalysts under CO_2 methanation reaction conditions: operando X-ray absorption and emission spectroscopy investigation, Appl. Catal. B Environ. 232 (2018) 409–419, https://doi.org/10.1016/j.apcatb.2018.03.089.
[15] G. Mishra, B. Dash, S. Pandey, Layered double hydroxides: a brief review from fundamentals to application as evolving biomaterials, Appl. Clay Sci. 153 (2018) 172–186, https://doi.org/10.1016/j.clay.2017.12.021.
[16] X. Liang, Y. Zang, Y. Xu, X. Tan, W. Hou, L. Wang, Y. Sun, Sorption of metal cations on layered double hydroxides, Colloids Surf. A Physicochem. Eng. Asp. 433 (2013) 122–131, https://doi.org/10.1016/j.colsurfa.2013.05.006.
[17] Z. Liu, X. Gao, B. Liu, Q. Ma, T. sheng Zhao, J. Zhang, Recent advances in thermal catalytic CO_2 methanation on hydrotalcite-derived catalysts, Fuel 321 (2022) 124115, https://doi.org/10.1016/j.fuel.2022.124115.
[18] X. Fang, C. Chen, H. Jia, Y. Li, J. Liu, Y. Wang, Y. Song, T. Du, L. Liu, Progress in adsorption-enhanced hydrogenation of CO_2 on layered double hydroxide (LDH) derived catalysts, J. Ind. Eng. Chem. 95 (2021) 16–27, https://doi.org/10.1016/j.jiec.2020.12.027.
[19] C.AbouI. Mallard, C. Poupin, M. Labaki, S. Siffert, R. Cousin, Ultraquick synthesis of hydrotalcite-like compounds as efficient catalysts for the oxidation of volatile organic compounds, Comptes Rendus Chim. 21 (2018) 993–1000, https://doi.org/10.1016/j.crci.2018.09.012.
[20] O.R. Macedo, N.F.P. Ribeiro, C.A.C. Perez, M. Schmal, M.M.V.M. Souza, Incorporation of cerium ions by sonication in Ni – Mg – Al layered double hydroxides, Appl. Clay Sci. 48 (2010) 542–546, https://doi.org/10.1016/j.clay.2010.02.015.
[21] F. Foroughi, J.J. Lamb, O.S. Burheim, B.G. Pollet, Sonochemical and sonoelectrochemical production of energy materials, Catalysts 11 (2021) 1–23, https://doi.org/10.3390/catal11020284.
[22] F. Ali, L. Reinert, J.M. Levêque, L. Duclaux, F. Muller, S. Saeed, S.S. Shah, Effect of sonication conditions: Solvent, time, temperature and reactor type on the preparation of micron sized vermiculite particles, Ultrason. Sonochem. 21 (2014) 1002–1009, https://doi.org/10.1016/j.ultsonch.2013.10.010.
[23] H. Kalawoun, M. Obeid, C. Ciotonea, M. Chaghouri, C. Poupin, S. Aouad, M. Labaki, C. Gennequin, E. Abi-Aad, F. Delattre, Review on the contribution of ultrasounds in layered double hydroxides synthesis and in their performances, Comptes Rendus Chim. 26 (2023) 167–179, https://doi.org/10.5802/crchim.249.
[24] E. Genty, J. Brunet, C. Poupin, S. Casale, S. Capelle, P. Massiani, S. Siffert, R. Cousin, Co-Al mixed oxides prepared via LDH route using microwaves or ultrasound: application for catalytic toluene total oxidation, Catalysts 5 (2015) 851–867, https://doi.org/10.3390/catal5020851.
[25] M. Muñoz, S. Moreno, R. Molina, Oxidative steam reforming of ethanol (OSRE) over stable NiCo–MgAl catalysts by microwave or sonication assisted coprecipitation, Int. J. Hydrog. Energy 42 (2017) 12284–12294, https://doi.org/10.1016/j.ijhydene.2017.03.090.
[26] M.J. Climent, A. Corma, S. Iborra, K. Epping, A. Velty, Increasing the basicity and catalytic activity of hydrotalcites by different synthesis procedures, J. Catal. 225 (2004) 316–326, https://doi.org/10.1016/j.jcat.2004.04.027.
[27] R.J. Chimentão, S. Abelló, F. Medina, J. Llorca, J.E. Sueiras, Y. Cesteros, P. Salagre, Defect-induced strategies for the creation of highly active hydrotalcites in base-catalyzed reactions, J. Catal. 252 (2007) 249–257, https://doi.org/10.1016/j.jcat.2007.09.015.
[28] S. Allahyari, M. Haghighi, A. Ebadi, S. Hosseinzadeh, Ultrasound assisted co-precipitation of nanostructured CuO-ZnO-Al_2O_3 over HZSM-5: effect of precursor and irradiation power on nanocatalyst properties and catalytic performance for direct syngas to DME, Ultrason. Sonochem. 21 (2014) 663–673, https://doi.org/10.1016/j.ultsonch.2013.09.014.
[29] Y. Vafaeian, M. Haghighi, S. Aghamohammadi, Ultrasound assisted dispersion of different amount of Ni over ZSM-5 used as nanostructured catalyst for hydrogen production via CO_2 reforming of methane, Energy Convers. Manag. 76 (2013) 1093–1103, https://doi.org/10.1016/j.enconman.2013.08.010.
[30] B.G. Pollet, The use of power ultrasound for the production of PEMFC and PEMWE catalysts and low-Pt loading and high-performing electrodes, Catalysts 9 (2019) 246, https://doi.org/10.3390/catal9030246.
[31] H.E. Hansen, F. Seland, S. Sunde, O.S. Burheim, B.G. Pollet, Two routes for sonochemical synthesis of platinum nanoparticles with narrow size distribution, Mater. Adv. 2 (2021) 1962–1971, https://doi.org/10.1039/d0ma00909a.
[32] H. Kalawoun, C. Ciotonea, M. Marinova, C. Gennequin, F. Delattre, Investigation of the physico-chemical properties of Ni-Mg-Al-La catalysts from ultrasound-assisted synthesis, Ultrason. Sonochem. 104 (2024), https://doi.org/10.1016/j.ultsonch.2024.106806.
[33] R. Singh Yadav, I. Kuřitka, J. Vilcakova, T. Jamatia, M. Machovsky, D. Skoda, P. Urbánek, M. Masař, M. Urbánek, L. Kalina, J. Havlica, Impact of sonochemical synthesis condition on the structural and physical properties of $MnFe_2O_4$ spinel ferrite nanoparticles, Ultrason. Sonochem. 61 (2020), https://doi.org/10.1016/j.ultsonch.2019.104839.
[34] T.S. Munonde, H. Zheng, The impact of ultrasonic parameters on the exfoliation of NiFe LDH nanosheets as electrocatalysts for the oxygen evolution reaction in alkaline media, Ultrason. Sonochem. 76 (2021) 105664, https://doi.org/10.1016/j.ultsonch.2021.105664.
[35] R. Benhiti, A. Ait Ichou, A. Zaghloul, R. Aziam, G. Carja, M. Zerbet, F. Sinan, M. Chiban, Synthesis, characterization, and comparative study of MgAl-LDHs prepared by standard coprecipitation and urea hydrolysis methods for phosphate removal, Environ. Sci. Pollut. Res. 27 (2020) 45767–45774, https://doi.org/10.1007/s11356-020-10444-5.
[36] F.L. Theiss, G.A. Ayoko, R.L. Frost, Synthesis of layered double hydroxides containing Mg^{2+}, Zn^{2+}, Ca^{2+} and Al^{3+} layer cations by co-precipitation methods - a review, Appl. Surf. Sci. 383 (2016) 200–213, https://doi.org/10.1016/j.apsusc.2016.04.150.
[37] C. Tanios, S. Bsaibes, C. Gennequin, M. Labaki, F. Cazier, S. Billet, H.L. Tidahy, B. Nsouli, A. Aboukaïs, E. Abi-Aad, Syngas production by the CO_2 reforming of CH_4 over Ni–Co–Mg–Al catalysts obtained from hydrotalcite precursors, Int. J. Hydrog. Energy 42 (2017) 12818–12828, https://doi.org/10.1016/j.ijhydene.2017.01.120.
[38] M.V. Bukhtiyarova, A review on effect of synthesis conditions on the formation of layered double hydroxides, J. Solid State Chem. 269 (2019) 494–506, https://doi.org/10.1016/j.jssc.2018.10.018.
[39] Y. Zhao, F. Li, R. Zhang, D.G. Evans, X. Duan, Preparation of layered double-hydroxide nanomaterials with a uniform crystallite size using a new method involving separate nucleation and aging steps, Chem. Mater. 14 (2002) 4286–4291, https://doi.org/10.1021/cm020370h.
[40] Q. Wang, H.H. Tay, Z. Guo, L. Chen, Y. Liu, J. Chang, Z. Zhong, J. Luo, A. Borgna, Morphology and composition controllable synthesis of Mg-Al-CO_3 hydrotalcites by tuning the synthesis pH and the CO_2 capture capacity, Appl. Clay Sci. 55 (2012) 18–26, https://doi.org/10.1016/j.clay.2011.07.024.
[41] H.S. Panda, R. Srivastava, D. Bahadur, Synthesis and in situ mechanism of nuclei growth of layered double hydroxides, Bull. Mater. Sci. 34 (2011) 1599–1604, https://doi.org/10.1007/s12034-011-0364-1.
[42] Z. Rong-jun, X.I.A. Guo-fu, L.I. Ming-feng, W.U. Yu, N.I.E. Hong, L.I. Da-dong, Effect of support on the performance of Ni-based catalyst in methane dry reforming, J. Fuel Chem. Technol. 43 (2015) 1359–1365, https://doi.org/10.1016/S1872-5813(15)30040-2.
[43] K. Wang, Y. Men, S. Liu, J. Wang, Y. Li, Y. Tang, Z. Li, W. An, X. Pan, L. Li, Decoupling the size and support/metal loadings effect of Ni/SiO2 catalysts for CO_2 methanation, Fuel 304 (2021) 121388, https://doi.org/10.1016/j.fuel.2021.121388.
[44] F.Z. Mahjoubi, A. Khalidi, O. Cherkaoui, R. Elmoubarki, M. Abdennouri, N. Barka, Treatment of textile effluents by chloride-intercalated Zn-, Mg- and Ni-Al layered double hydroxides, J. Water Reuse Desalin. 7 (2017) 307–318, https://doi.org/10.2166/wrd.2016.041.
[45] L. Shi, Z. Zhang, R. Wang, C. Zhou, C. Sun, Study on ultrasound-assisted precipitation for preparing Ni/Al_2O_3 catalyst, Ultrason. Sonochem. 67 (2020) 105107, https://doi.org/10.1016/j.ultsonch.2020.105107.
[46] S. Moreno, M. Munoz, R. Molina, Synthesis of Ce and Pr-promoted Ni and Co catalysts from hydrotalcite type precursors by reconstruction method, Int. J. Hydrog. Energy 37 (2012) 18827–18842, https://doi.org/10.1016/j.ijhydene.2012.09.132.
[47] U. Sikander, S. Sufian, M.A. Salam, A review of hydrotalcite based catalysts for hydrogen production systems, Int. J. Hydrog. Energy 42 (2017) 19851–19868, https://doi.org/10.1016/j.ijhydene.2017.06.089.
[48] R. Dębek, M.E. Galvez, F. Launay, M. Motak, T. Grzybek, P. Da Costa, Low temperature dry methane reforming over Ce, Zr and CeZr promoted Ni–Mg–Al hydrotalcite-derived catalysts, Int. J. Hydrog. Energy 41 (2016) 11616–11623, https://doi.org/10.1016/j.ijhydene.2016.02.074.
[49] F. Rouquerol, J. Rouquerol, K.S.W. Sing, P. Lewellyn, G. Maurin, Adsorption by Powders and Porous Solids: Principle, Methodology and Applications, 2nd editio, Academic Press, New York, 2013.
[50] M. Thommes, K.A. Cychosz, Physical adsorption characterization of nanoporous materials: progress and challenges, Adsorption 20 (2014) 233–250, https://doi.org/10.1007/s10450-014-9606-z.
[51] J. Wang, S. Yang, H. Sun, J. Qiu, Y. Men, Highly improved soot combustion performance over synergetic $Mn_xCe_{1-x}O_2$ solid solutions within mesoporous nanosheets, J. Colloid Interface Sci. 577 (2020) 355–367, https://doi.org/10.1016/j.jcis.2020.05.090.
[52] F. Rahbar Shamskar, F. Meshkani, M. Rezaei, Ultrasound assisted co-precipitation synthesis and catalytic performance of mesoporous nanocrystalline NiO-Al_2O_3 powders, Ultrason. Sonochem. 34 (2017) 436–447, https://doi.org/10.1016/j.ultsonch.2016.06.021.
[53] S. Zhuang, Z. Hu, L. Huang, F. Qin, Z. Huang, C. Sun, W. Shen, H. Xu, Synthesis of ZSM-5 catalysts with tunable mesoporosity by ultrasound-assisted method: a highly stable catalyst for methanol to propylene, Catal. Commun. 114 (2018) 28–32, https://doi.org/10.1016/j.catcom.2018.06.001.
[54] H. Nguyen-Phu, T. Kim, Y. Kim, K.H. Kang, H. Cho, J. Kim, I. Ro, Role of phase in NiMgAl mixed oxide catalysts for CO_2 dry methane reforming (DRM), Catal. Today (2022), https://doi.org/10.1016/j.cattod.2022.08.036.
[55] C. Mebrahtu, F. Krebs, S. Perathoner, S. Abate, G. Centi, R. Palkovits, Hydrotalcite based Ni-Fe/(Mg, Al)O_X catalysts for CO_2 methanation-tailoring Fe content for

improved CO dissociation, basicity, and particle size, Catal. Sci. Technol. 8 (2018) 1016–1027, https://doi.org/10.1039/c7cy02099f.
[56] R. Dębek, K. Zubek, M. Motak, M.E. Galvez, P. Da Costa, T. Grzybek, Ni-Al hydrotalcite-like material as the catalyst precursors for the dry reforming of methane at low temperature, Comptes Rendus Chim. 18 (2015) 1205–1210, https://doi.org/10.1016/j.crci.2015.04.005.
[57] U. Kunz, C. Binder, U. Hoffmann, Preparation of fine particles as catalysts and catalyst precursors by the use of ultrasound during precipitation, 1995.
[58] A. Borodziński, M. Bonarowska, Relation between crystallite size and dispersion on supported metal catalysts, Langmuir 13 (1997) 5613–5620, https://doi.org/10.1021/la962103u.
[59] O. Daoura, G. Fornasieri, M. Boutros, N. El Hassan, P. Beaunier, C. Thomas, M. Selmane, A. Miche, C. Sassoye, O. Ersen, W. Baaziz, P. Massiani, A. Bleuzen, F. Launay, One-pot prepared mesoporous silica SBA-15-like monoliths with embedded Ni particles as selective and stable catalysts for methane dry reforming, Appl. Catal. B Environ. 280 (2021) 119417, https://doi.org/10.1016/j.apcatb.2020.119417.
[60] R. Razzaq, C. Li, N. Amin, S. Zhang, K. Suzuki, Co-methanation of carbon oxides over nickel-based $Ce_xZr_{1-x}O_2$ catalysts, Energy Fuels 27 (2013) 6955–6961.
[61] K.S. Suslick, M.M. Fang, T. Hyeon, M.M. Mdleleni, Applications of Sonochemistry to Materials Synthesis, Eds. Dordr, 1999.
[62] M.S.W. Lim, T.C.K. Yang, T.J. Tiong, G.T. Pan, S. Chong, Y.H. Yap, Ultrasound-assisted sequentially precipitated nickel-silica catalysts and its application in the partial hydrogenation of edible oil, Ultrason. Sonochem. 73 (2021) 105490, https://doi.org/10.1016/j.ultsonch.2021.105490.
[63] M.S.W. Lim, T.C.K. Yang, Y.H. Yap, G.T. Pan, S. Chong, T.J. Tiong, Intensification and optimisation of nickel recovery from spent hydrogenation catalysts via ultrasound-augmented hydrometallurgy, J. Environ. Chem. Eng. 9 (2021) 105771, https://doi.org/10.1016/j.jece.2021.105771.
[64] H. Zhang, M. Li, P. Xiao, D. Liu, C.J. Zou, Structure and catalytic performance of Mg-SBA-15-supported nickel catalysts for CO_2 reforming of methane to syngas, Chem. Eng. Technol. 36 (2013) 1701–1707, https://doi.org/10.1002/ceat.201300006.
[65] C.I. Ezeh, X. Huang, X. Yang, C. gong Sun, J. Wang, Sonochemical surface functionalization of exfoliated LDH: effect on textural properties, CO_2 adsorption, cyclic regeneration capacities and subsequent gas uptake for simultaneous methanol synthesis, Ultrason. Sonochem. 39 (2017) 330–343, https://doi.org/10.1016/j.ultsonch.2017.04.041.
[66] S.I. Garcés-Polo, J. Villarroel-Rocha, K. Sapag, S.A. Korili, A. Gil, Adsorption of CO_2 on mixed oxides derived from hydrotalcites at several temperatures and high pressures, Chem. Eng. J. 332 (2018) 24–32, https://doi.org/10.1016/j.cej.2017.09.056.
[67] P. Hongmanorom, J. Ashok, G. Zhang, Z. Bian, M.H. Wai, Y. Zeng, S. Xi, A. Borgna, S. Kawi, Enhanced performance and selectivity of CO_2 methanation over phyllosilicate structure derived Ni-Mg/SBA-15 catalysts, Appl. Catal. B Environ. 282 (2021) 119564, https://doi.org/10.1016/j.apcatb.2020.119564.
[68] Q. Pan, J. Peng, T. Sun, S. Wang, S. Wang, Insight into the reaction route of CO_2 methanation: promotion effect of medium basic sites, Catal. Commun. 45 (2014) 74–78, https://doi.org/10.1016/j.catcom.2013.10.034.
[69] M.C. Biesinger, B.P. Payne, L.W.M. Lau, A. Gerson, R.S.C. Smart, X-ray photoelectron spectroscopic chemical state Quantification of mixed nickel metal, oxide and hydroxide systems, Surf. Interface Anal. 41 (2009) 324–332, https://doi.org/10.1002/sia.3026.
[70] C. Zhang, J. Wang, S. Yang, H. Liang, Y. Men, Boosting total oxidation of acetone over spinel MCo_2O_4 (M = Co, Ni, Cu) hollow mesoporous spheres by cation-substituting effect, J. Colloid Interface Sci. 539 (2019) 65–75, https://doi.org/10.1016/j.jcis.2018.12.061.
[71] G. Zhai, J. Wang, Z. Chen, W. An, Y. Men, Boosting soot combustion efficiency of Co_3O_4 nanocrystals via tailoring crystal facets, Chem. Eng. J. 337 (2018) 488–498, https://doi.org/10.1016/j.cej.2017.12.141.
[72] R.B. Shalvoy, B.H. Davis, P.J. Reucroft, Studies of the metal–support interaction in coprecipitated nickel on alumina methanation catalysts using X-ray photoelectron spectroscopy (XPS), Surf. Interface Anal. 2 (1980) 11–16, https://doi.org/10.1002/sia.740020104.
[73] C. Alvarez-Galvan, M. Melian, L. Ruiz-Matas, J.L. Eslava, R.M. Navarro, M. Ahmadi, B.R. Cuenya, J.L.G. Fierro, Partial oxidation of methane to syngas over nickel-based catalysts: Influence of support type, addition of rhodium, and preparation method, Front. Chem. 7 (2019) 1–16, https://doi.org/10.3389/fchem.2019.00104.
[74] J. Lu, Y. Lei, G. Wan, Z. Mei, J. Yu, Y. Zhao, S. He, Y. Luo, Weakening the metal-support strong interaction to enhance catalytic performances of alumina supported Ni-based catalysts for producing hydrogen, Appl. Catal. B Environ. 263 (2020) 118177, https://doi.org/10.1016/j.apcatb.2019.118177.
[75] H. Li, C.J. Ma, H.X. Li, Ultrasound-assisted cinnamaldehyde hydrogenation to cinnamyl alcohol at atmospheric pressure over Ru-B amorphous catalyst, Chin. J. Chem. 24 (2006) 613–619, https://doi.org/10.1002/cjoc.200690118.
[76] S. Xu, X. Wang, Highly active and coking resistant Ni/CeO_2-ZrO_2 catalyst for partial oxidation of methane, Fuel 84 (2005) 563–567, https://doi.org/10.1016/j.fuel.2004.10.008.
[77] I. Sreedhar, Y. Varun, S.A. Singh, A. Venugopal, B.M. Reddy, Developmental trends in CO_2 methanation using various catalysts, Catal. Sci. Technol. 9 (2019) 4478–4504, https://doi.org/10.1039/c9cy01234f.
[78] I. Fechete, J.C. Vedrine, Nanoporous materials as new engineered catalysts for the synthesis of green fuels, Molecules 20 (2015) 5638–5666, https://doi.org/10.3390/molecules20045638.
[79] X. Xu, Y. Tong, J. Huang, J. Zhu, X. Fang, J. Xu, X. Wang, Insights into CO_2 methanation mechanism on cubic ZrO_2 supported Ni catalyst via a combination of experiments and DFT calculations, Fuel 283 (2021) 118867, https://doi.org/10.1016/j.fuel.2020.118867.
[80] E. Baraj, S. Vagaský, T. Hlinčik, K. Ciahotný, V. Tekáč, Reaction mechanisms of carbon dioxide methanation, Chem. Pap. 70 (2016) 395–403, https://doi.org/10.1515/chempap-2015-0216.
[81] Z. Wang, T. Zhang, T. Ramirez Reina, L. Huang, W. Xie, N.M. Musyoka, B. Oboirien, Q. Wang, Enhanced low-temperature CO_2 methanation over La-promoted NiMgAl LDH derived catalyst: fine-tuning La loading for an optimal performance, Fuel 366 (2024) 131383–131395, https://doi.org/10.1016/j.fuel.2024.131383.
[82] K. Ray, G. Deo, A potential descriptor for the CO_2 hydrogenation to CH_4 over Al_2O_3 supported Ni and Ni-based alloy catalysts, Appl. Catal. B Environ. 218 (2017) 525–537, https://doi.org/10.1016/j.apcatb.2017.07.009.
[83] M. Boudart, Turnover rates in heterogeneous catalysis, Chem. Rev. 95 (1995) 661–666, https://doi.org/10.1021/cr00035a009.
[84] X. Jia, X. Zhang, N. Rui, X. Hu, C. jun Liu, Structural effect of Ni/ZrO_2 catalyst on CO_2 methanation with enhanced activity, Appl. Catal. B Environ. 244 (2019) 159–169, https://doi.org/10.1016/j.apcatb.2018.11.024.
[85] M. Obeid, C. Poupin, M. Labaki, S. Aouad, F. Delattre, S. Gupta, H. Lucette Tidahy, A. Younis, F. Ben Romdhane, E.M. Gaigneaux, J. Schnee, E. Abi-Aad, CO_2 methanation over LDH derived NiMgAl and NiMgAlFe oxides: improving activity at lower temperatures via an ultrasound-assisted preparation, Chem. Eng. J. 474 (2023) 145460, https://doi.org/10.1016/j.cej.2023.145460.
[86] D. Wierzbicki, R. Baran, R. Dębek, M. Motak, T. Grzybek, M.E. Gálvez, P. Da Costa, The influence of nickel content on the performance of hydrotalcite-derived catalysts in CO_2 methanation reaction, Int. J. Hydrog. Energy 42 (2017) 23548–23555, https://doi.org/10.1016/j.ijhydene.2017.02.148.
[87] N. Bette, J. Thielemann, M. Schreiner, F. Mertens, Methanation of CO_2 over a (Mg, Al)O_x supported nickel catalyst derived from a (Ni, Mg, Al) -hydrotalcite-like precursor, Chemcatchem Commun. 8 (2016) 2903, https://doi.org/10.1002/cctc.201600469.
[88] Y.R. Dias, O.W. Perez-Lopez, CO_2 methanation over Ni-Al LDH-derived catalyst with variable Ni/Al ratio, J. CO_2 Util. 68 (2023) 102381, https://doi.org/10.1016/j.jcou.2022.102381.
[89] D. Wierzbicki, M.V. Moreno, S. Ognier, M. Motak, T. Grzybek, P. Da Costa, M. E. Gálvez, Ni-Fe layered double hydroxide derived catalysts for non-plasma and DBD plasma-assisted CO_2 methanation, Int. J. Hydrog. Energy 45 (2020) 10423–10432, https://doi.org/10.1016/j.ijhydene.2019.06.095.